An ultrafast 2-D non-resonant cutting tool for texturing micro-structured surfaces

Jianjian Wang[a,b,c], Hanheng Du[b], Shiming Gao[b], Yang Yang[b], Zhiwei Zhu[d], Ping Guo[a,*]

[a] Department of Mechanical Engineering, Northwestern University, Evanston, IL, USA
[b] Department of Mechanical and Automation Engineering, The Chinese University of Hong Kong, Hong Kong, China
[c] Shun Hing Institute of Advanced Engineering, The Chinese University of Hong Kong, Hong Kong, China
[d] School of Mechanical Engineering, Nanjing University of Science and Technology, Nanjing, China

ARTICLE INFO

ABSTRACT

Surface texturing using two-dimensional non-resonant vibration cutting tools (2-D NRVCT) has emerged as a promising method to fabricate micro-structured surfaces. The non-resonant vibration tool is able to work in a continuous frequency range with precise control of the tool trajectories compared with their resonant counterparts. The existing designs, however, usually suffer from either small vibration amplitudes or a low bandwidth due to a set of contradictory design requirements. This study presents a tool design that features a high bandwidth of up to 6 kHz without extra cooling, a working space of 9.3 μm × 16 μm, and a small cross-axis coupling within 5%. In addition, this study attempts to generalize the design requirements for 2-D non-resonant vibration cutting tools in five key functional specifications, including the stroke, output stiffness, resonant frequency, drive current, and coupling coefficient. Analytical modeling of the working performance on structural stiffness and output strokes using the compliance matrix method is presented and verified by finite element analysis. Dimensions of the proposed design have been optimized to achieve a balance between the amplification ratio and the bandwidth. The tool performance is then experimentally evaluated along with surface texturing results using the elliptical, quadrate and modulated elliptical tool trajectories.

1. Introduction

Structured surfaces with regular micro/nano textures represent a new trend of promising technologies for enhancing functionality and performance of industrial components in terms of their tribological [1], biological [2], mechanical [3], optical [4] and other properties [5]. How to fabricate these surfaces with high efficiency, low cost and high flexibility has attracted an enormous amount of attention in both academia and industry [6]. Laser ablation is favorable for its flexibility, but is usually limited to prototyping due to its high cost and long processing time. It is also limited to processing non-transparent materials and requires further post-processing operations [7]. The micro forming method is ideal for mass production, but is less applicable to high strength and brittle materials. Besides, how to manufacture the molds and dies with micro-features remains a problem [8]. Micro-machining with diamond tools is well suited at this length-scale and offers great advantage of its flexibility – nearly no limitation on work materials [9]. It could also obtain a nanometric surface finish that requires no post-processing. Diamond machining also increases geometric accuracy by

eliminating remounting and any further polishing operations. Currently, however, the conventional way to machine 3D micro-features is by 5-axis numerically controlled machining. Diamond micro-machining, though highly accurate, is still not satisfactory in efficiency for mass production.

To overcome the aforementioned problems, surface shaping utilizing tertiary tool motion was proposed to machine structured surfaces [10]. The tool tertiary motion is usually a high-frequency periodic motion, given by either a resonant or non-resonant vibration generator. The resonant motion generator utilizes the amplification of resonant vibration of the structure to obtain large amplitudes at a higher frequency. Examples include ultrasonic elliptical vibration cutting tools by coupling two orthogonal resonant modes [8,11,12]. Though operating at an ultrasonic frequency, these resonant mode vibration generators only work at a fixed frequency. They also lack precise control of the tool trajectories due to the nature of resonant vibration, which has a profound impact on the microstructure topography and its functional performance.

On the other hand, non-resonant vibration generators could work in

---

* Corresponding author.
  E-mail address: ping.guo@northwestern.edu (P. Guo).

a continuous frequency range with precise control of the tool trajectories. In recent years, many attempts have shifted towards the design of 2-D non-resonant vibration cutting tools (NRVCT). Ahn et al. developed a 2-D NRVCT that operated at 1 kHz with strokes of 5 μm × 5 μm by using two perpendicularly arranged piezoelectric stacks to actuate a flexure hinge block [13]. Heamawatanachai and Bamberg developed a micromachining tool, which could generate 2-D vibration with amplitudes of 10 μm × 10 μm at 300 Hz [14] by using a bending-mode piezoelectric tube. However, this design is not suitable for elliptical vibration cutting due to its low stiffness. Negishi and Dow developed two kinds of 2-D non-resonant vibrators that can work at low frequency and high frequency respectively. The low-frequency design used air cooling for the piezoelectric stacks and worked between 0–400 Hz [15], while the high-frequency design used a liquid cooling system to ramp the working bandwidth to 4 kHz [15]. Zhu et al. proposed a 2-D non-resonant cutting tool with decoupled kinematics using Z-shaped flexure hinges, which can operate at 200 Hz with a stroke of 15 μm [16]. Lin et al. developed a 2-D piezoelectric tool actuator based on a hybrid flexure hinge mechanism, which can work at 500 Hz with a stroke of 15 μm [17].

The maximal operating frequency and stroke of the previous designs are summarized in Fig. 1. The solid line in Fig. 1 represents the inverse relationship between the stroke and the maximal working frequency, which indicates that a large motion stroke and a high bandwidth are very difficult to achieve simultaneously. These existing 2-D NRVCTs usually suffer from small vibration amplitudes or low working frequency, which affects either the machining flexibility or efficiency in micro-scale surface texturing. These restrictions result from the intrinsic working principle of piezoelectric actuators. Both the drive current for a piezo stack actuator and its heat generation increase with the actuator capacitance, excitation frequency, and input voltage. In order to achieve a large amplitude at a high working frequency, not only a high-power piezo amplifier but also an extra cooling system are usually required. However, the high-power piezo amplifier is not readily available on the market, and the extra cooling system makes the tool design bulky and unreliable. Moreover, the frequency bandwidth of the 2-D NRVCT is often limited by the first natural frequency of the mechanical structure. When reducing the structural size to achieve a higher resonant frequency, the displacement outputs will also fall short. A mechanical amplification mechanism is thus needed to amplify the output displacement of the piezo stacks, which in turn lowers the tool stiffness and the structural resonant frequency. All these contradictory requirements make it difficult to optimize the tool design.

In an attempt to address to these challenges in the tool design of 2-D NRVCT, this paper presents a tool design in order to achieve a performance balance among the five k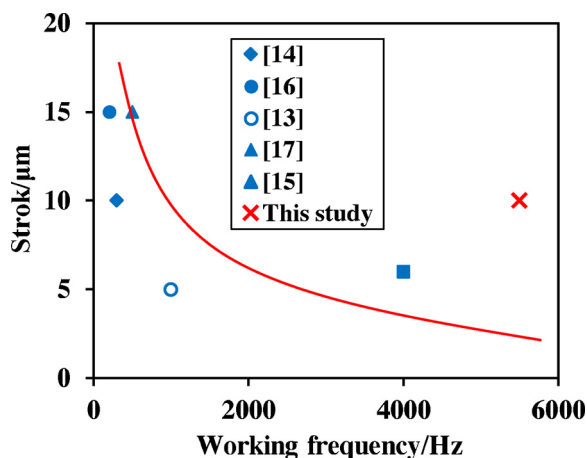ey specifications, including the stroke, the output stiffness, resonant frequency, drive current, and coupling coefficient. More specifically, the proposed tool is capable to produce decoupled 2-D motions of at least 10 μm in each direction with a bandwidth up to 6 kHz without extra cooling. Considering the direct application of the tool in machining micro-structured surfaces, the open loop output stiffness is targeted at several hundreds of mN per micron in the cutting direction; and greater than 1 N/μm in the thrust direction.

Not only focusing on specific tool design, but this paper also presents a general design guideline and modeling techniques for flexure-hinge based 2-D tool design for high-frequency operation. We also attempt to generalize the design requirements for micro-machining in five key specifications (stroke, output stiffness, resonant frequency, drive current, and coupling coefficient) and discuss their relationships with the design space. To our best of knowledge, this is the very few attempts to present the tool design in a holistic approach to include the modeling and consideration of all functional requirements. We first present the mechanical design in Section 2, along with the analytical modeling and optimization in Section 3. Experimental verification of the tool performance and surface texturing results are demonstrated in Section 4. A short conclusion is given at the end.

2. Mechanical design

The general approach adopted in this design is to utilize a modified bridge-type amplification mechanism with a small amplification ratio to balance the requirements among the stroke, output stiffness, resonant frequency, and the drive current. A pair of bridge-type mechanisms are connected by two perpendicular leaf-spring flexure hinges to decouple the 2-D motion, while the end effector is kept at a minimum weight to increase its first resonant frequency. The motion generation principle of the proposed 2-D NRVCT is clarified by the kinematic diagram as illustrated in Fig. 2, where u_{in}^{left} and u_{in}^{right} are the input displacements from two piezo stack actuators (PSAs) respectively. By actuating two PSAs independently, 2-D amplified motions at the tool tip can be generated in the cutting plane, namely the xy plane.

The design details of the proposed 2-D NRVCT are further illustrated in Fig. 3(a). Spring steel is chosen as the main material due to its high elasticity and fatigue strength. The design also considers the manufacturability, so that the monolithic design can be machined by wire electrical discharge machining (EDM) from a single workpiece. The overall dimensions are 30 mm × 30 mm × 6 mm. Two kinds of basic flexure hinges are utilized in the design, namely the right circular flexure hinge (RCFH) and the leaf-spring flexure hinge (LSFH) as depicted in Fig. 3(b) and (c). Important geometric parameters include b, the thickness of NRVCT; t and R, the neck thickness and radius of RCFH; and $w_1(w_2)$ and $h_1(h_2)$, the width and length of LSFH1 (LSFH2). The RCFH serves as a revolute pair to magnify the input motion of piezo stack actuators (PSAs), while the LSFH only transmits one-directional translation to decouple the cross-coupling motion.
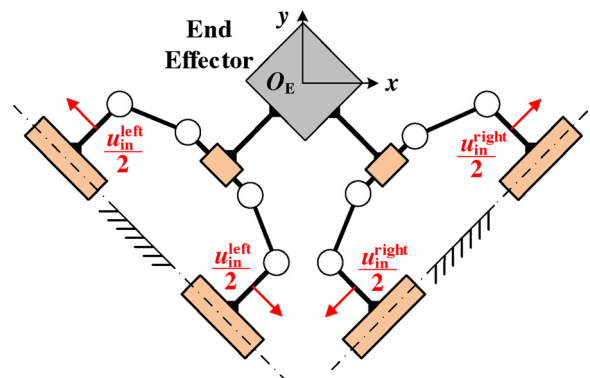

Fig. 1. Comparison of the proposed 2-D NRVCT with existing designs in terms of frequency and stroke.

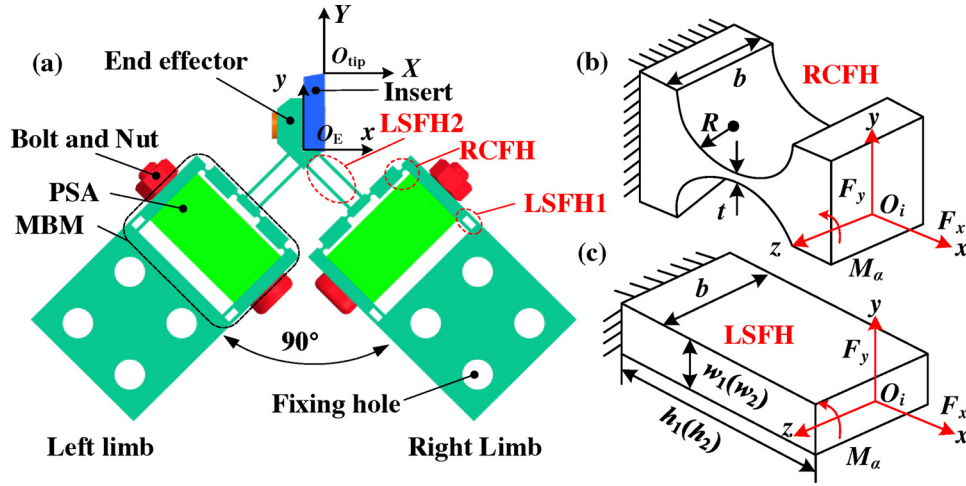**Fig. 2.** Kinematic diagram of the designed NRVCT.

Fig. 3. Design of the 2-D NRVCT: (a) mechanical structure; schematics of (b) right circular flexure hinge (RCFH) and (c) leaf-spring flexure hinge (LSFH).

As shown in Fig. 3(a), the designed tool mainly consists of two symmetric limbs. Each limb includes a modified bridge-type displacement amplifier mechanism (MBM) actuated by a PSA. The MBM is not a usual symmetric configuration as used in other research [18]. It consists of only the top half of a typical bridge-type mechanism, but the bottom half is replaced with two pairs of parallel LSFH mechanisms (LSFH1 in Fig. 3 = (a)) for a more compact design and increased structural resonant frequency. The motion outputs from the MBM are decoupled by the other two sets of parallel LSFH mechanisms (LSFH2 in Fig. 3(a)), which are connected at 90° by an end effector. A triangular insert is mounted on the end effector, which is compatible with commercially available triangular indexable inserts.

3. Performance modeling and analysis

In this section, we present the analytical models to obtain a general relationship between the design parameters and the motion stroke and output stiffness. We evaluate all the five performance requirements of the stroke, output stiffness, resonant frequency, drive current, and coupling coefficient; and the tool geometry is optimized by balancing all the requirements and the manufacturing practicality.

3.1. Output stiffness

The output stiffness can be defined as the ratio between the cutting force (in the cutting and thrust directions) and the displacement of the tool tip. The tool tip should be able to follow the prescribed trajectory accurately under the external disturbance of cutting force. The direct application of proposed tool is in micro surface texturing, where the expected cutting force is in the range from tens to hundreds of milli-newtons (mN) [19]. The design goal is to have the output stiffness to be at least of hundreds of mN per micron and to have a significantly higher stiffness in the thrust direction, which affects the accuracy of machined micro-structures most. It should be noted that the actual tool output stiffness could be further improved by adopting a feedback control loop, which will be considered in our future work.

The geometric definition of the left limb is illustrated in Fig. 4, which includes an MBM and LSFH2. Due to the symmetry of MBM, the left part is annotated with all the geometric parameters ($L_1 - L_7$) and coordination definitions incorporated in the modeling. There are six flexure hinges, including two RCFHs (Hinge 3 and 4) and four LSFHs (Hinge 1, 2, 5 and 6) and their corresponding output ends ($O_1 - O_6$). Since the bolts to mount the PSAs also have significant impacts on the structure stiffness, the bolt stiffness k_{bolt} is also be included in the stiffness modeling of NRVCT.

Considering the designed 2-D NRVCT is mainly constructed by

flexure hinges, the compliance-based matrix method can be used to model the output stiffness [20]. For the two basic flexure hinge units, RCFH and LSFH, shown in Fig. 3(b) and (c), assuming that a general force vector $[F_x, F_y, M_\alpha]$ is applied to the free end O_i, a corresponding displacement vector $[\Delta x, \Delta y, \Delta \alpha]$ at this end will be generated. Their relationship can be expressed as a local compliance matrix C_h as:

$$
\mathbf{C}_h = \begin{bmatrix} \dfrac{\Delta x}{F_x} & 0 & 0 \\ 0 & \dfrac{\Delta y}{F_y} & \dfrac{\Delta y}{M_\alpha} \\ 0 & \dfrac{\Delta \alpha}{F_y} & \dfrac{\Delta \alpha}{M_\alpha} \end{bmatrix}
\tag{1}
$$

The elements of this 3×3 matrix are functions of the structure parameters and material properties including the neck thickness t of the flexure hinges, which are defined in [21] and [22]. The local compliance matrix of the hinge is defined as $C_i^0 = C_h$, where "0" indicates the global ground coordinate that will be omitted throughout this paper. The compliance C_i can be transferred into another frame O_j by

$$
\mathbf{C}_i^j = \mathbf{T}_i^j \cdot \mathbf{C}_i \cdot (\mathbf{T}_i^j)^T
\tag{2}
$$

where the transformation matrix takes on the following form:

$$
\mathbf{T}_i^j = \mathbf{T}(\theta, \mathbf{r}_i^j) = \begin{bmatrix} \cos\theta & \sin\theta & r_y \\ -\sin\theta & \cos\theta & -r_x \\ 0 & 0 & 1 \end{bmatrix}
\tag{3}
$$

where θ is the rotation angle of coordinate O_i with respect to O_j; $\mathbf{r}_i^j = (r_x, r_y)^T$ is the position vector of O_i expressed in the reference frame O_j.

Firstly, the compliance matrix of the left half of MBM at point O_{R1} with respect to the ground can be derived as:

$$
\mathbf{C}_{R1\_left} = ((\mathbf{C}_1^{R1})^{-1} + (\mathbf{C}_2^{R1})^{-1} + \mathbf{K}_{bolt}^{R1})^{-1} + \mathbf{C}_3^{R1} + \mathbf{C}_4^{R1}
\tag{4}
$$

where K_{bolt}^{R1} is the stiffness matrix of the bolt expressed in $xO_{R1}y$, which can be calculated by

$$
\mathbf{K}_{bolt}^{R1} = \mathbf{T}(\pi/2, \mathbf{r}_{bolt}^{R1})^{-T} \cdot \mathbf{K}_{bolt} \cdot \mathbf{T}(\pi/2, \mathbf{r}_{bolt}^{R1})^{-1}
\tag{5}
$$

where K_{bolt} is the 2-by-2 stiffness matrix in its local coordinate system. The only non-zero element in $\mathbf{K}_{bolt}$ is $K_{bolt}(2,2) = 2k_{bolt}$. k_{bolt} is the tensile stiffness of the bolt.

Due to the left-right symmetry of the MBM, the compliance matrix C_{R1} of the whole MBM at O_{R1} with respect to the ground can be obtained as:

$$
\mathbf{C}_{R1} = ((\mathbf{C}_{R1\_left})^{-1} + (\mathbf{T}_y \cdot \mathbf{C}_{R1\_left} \cdot (\mathbf{T}_y)^T)^{-1})^{-1}
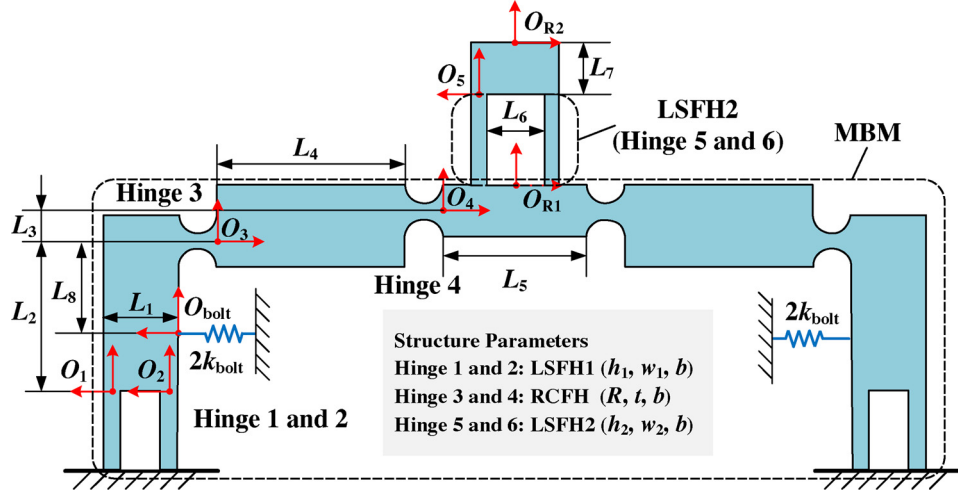\tag{6}
$$

Fig. 4. Definition of geometric parameters and coordinates of the left limb of NRVCT for the calculation of output stiffness.

with the transformation matrix mirroring the left half as:

$$\mathbf{T}_y = \begin{bmatrix} -1 & 0 & 0 \\ 0 & 1 & 0 \\ 0 & 0 & -1 \end{bmatrix} \qquad (7)$$

The compliance matrix of the total limb is then the summation of $\mathbf{C}_{R1}$ and the compliance matrix of LSFH2, which is given by

$$\mathbf{C}^{R2} = ((\mathbf{T}_y \cdot \mathbf{C}_5^{R2} \cdot \mathbf{T}_y^T)^{-1} + (\mathbf{C}_5^{R2})^{-1})^{-1} + \mathbf{C}_{R1}^{R2} \qquad (8)$$

We then transform the above compliance matrix into the global frame O_E (as defined in Fig. 3) as:

$$\mathbf{C}_{\text{left}}^E = \mathbf{T}(-\pi/4, \mathbf{0}) \cdot \mathbf{C}_{R2} \cdot \mathbf{T}(-\pi/4, \mathbf{0})^T \qquad (9)$$

Due to the left-right symmetry of the designed tool, the compliance matrix of the entire tool at O_E with respect to the ground can be calculated by

$$\mathbf{C}_E = ((\mathbf{C}_{\text{left}}^E)^{-1} + (\mathbf{T}_y \cdot \mathbf{C}_{\text{left}}^E \cdot \mathbf{T}_y^T)^{-1})^{-1} \qquad (10)$$

Then the compliance matrix at tool tip expressed in frame O_{tip} that is located at the tool tip as shown in Fig. 3 can be obtained as:

$$\mathbf{C}_{\text{tip}} = \mathbf{T}(0, \mathbf{r}_E^{\text{tip}}) \cdot \mathbf{C}_E \cdot \mathbf{T}(0, \mathbf{r}_E^{\text{tip}})^T \qquad (11)$$

Finally, the output stiffness at the tool tip in the cutting direction, K_{out}^x, and in the thrust direction, K_{out}^y, can be derived by the definition as:

$$\begin{cases} \mathbf{u}_x = \mathbf{C}_{\text{tip}} \times (F_x, 0, 0)^T, & K_{\text{out}}^x = F_x / \mathbf{u}_x(1) \\ \mathbf{u}_y = \mathbf{C}_{\text{tip}} \times (0, F_y, 0)^T, & K_{\text{out}}^y = F_y / \mathbf{u}_y(2) \end{cases} \qquad (12)$$

3.2. Output stroke

The actual output motions of tool tip are not only governed by the geometrical configuration, but also related to the structure input stiffness considering the finite force output from PSAs. Thus, it is essential to model the input stiffness and the amplification ratio to accurately determine the tool output strokes. Due to symmetry, only the left part of one MBM is illustrated in Fig. 5, where O_{in} is the input point of actuation force F_{in} from the PSA; c_0 is the compliance of vertical spring in Fig. 5, which is used to represent the compliance of the right limb. Its compliance c_0 can be obtained by

$$c_0 = 2(\mathbf{C}_{R2}(1, 1) + \mathbf{C}_{\text{LSFH2}}(1, 1)/2) \qquad (13)$$

where C_{LSFH2} is the local compliance matrix of LSFH2. The compliance matrix $\mathbf{C}_S$ of the vertical spring in Fig. 5 expressed in its local frame at O_S can be written as:
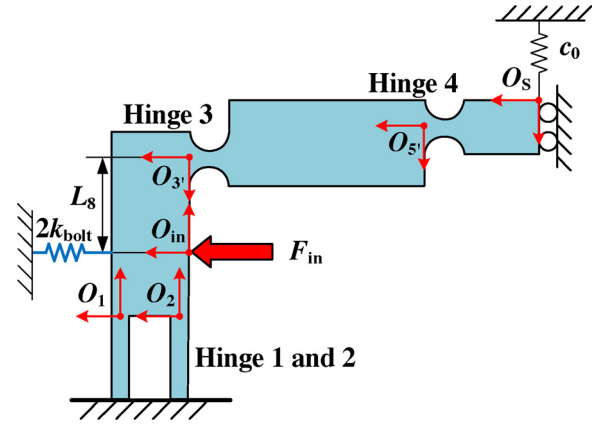

Fig. 5. Definition of geometric parameters and coordinates of half of the left limb for the calculation of input stiffness.

$$\mathbf{C}_S = \begin{bmatrix} 0 & 0 & 0 \\ 0 & c_0 & 0 \\ 0 & 0 & 0 \end{bmatrix} \qquad (14)$$

Then the input compliance matrix $\mathbf{C}_{\text{in}}$ at O_{in} expressed in its local frame can be derived as:

$$\mathbf{C}_{\text{in}} = ((\mathbf{C}_S^{\text{in}} + \mathbf{C}_{4'}^{\text{in}} + \mathbf{C}_{3'}^{\text{in}})^{-1} + (\mathbf{C}_1^{\text{in}})^{-1} + (\mathbf{C}_2^{\text{in}})^{-1})^{-1} \qquad (15)$$

where C_i^{in} is the compliance matrix of the corresponding flexure hinge derived according to Eq. (1) and Eq. (2).

The input stiffness of the designed tool can be obtained as

$$K_{\text{in}} = (1/\mathbf{C}_{\text{in}}(2, 2) + 2k_{\text{bolt}})/2 \qquad (16)$$

In addition, in order to guarantee that no significant bending moment is exerted on the PSA during its extension, the following inequality should be satisfied,

$$2 \cdot \mathbf{C}_{\text{in}}(3, 2) \cdot L_8 / \mathbf{C}_{\text{in}}(2, 2) < e_0 \qquad (17)$$

where e_0 is set as 5% in this study.

When an input force $\mathbf{F}_{\text{in}} = (0, F_{\text{in}}, 0)^T$ acts on O_{in}, the input displacement vector can be calculated by $\mathbf{U}_{\text{in}} = \mathbf{C}_{\text{in}} \mathbf{F}_{\text{in}}$, so the input displacement along the F_{in} direction as shown in Fig. 5 can be obtained as $u_{\text{in}} = 2\mathbf{U}_{\text{in}}(2)$.

The displacement vector $\mathbf{U}_{3'}$ at $O_{3'}$ under the actuation force F_{in} can be derived as:

$$\mathbf{U}_{3'} = \mathbf{T}(\pi/2, \mathbf{r}_{3'}^{\text{in}})^{-1} \mathbf{U}_{\text{in}} \qquad (18)$$

The compliance matrix $\mathbf{C}_{3'}$ at $O_{3'}$ contributed by Hinge 3 and Hinge 4 can be written as:

$$\mathbf{C}_{3'} = \mathbf{T}(\pi/2, \mathbf{r}_{3'}^{\text{in}})^{-1}(\mathbf{C}_s^{\text{in}} + \mathbf{C}_{3'}^{\text{in}} + \mathbf{C}_{4'}^{\text{in}})\mathbf{T}(\pi/2, \mathbf{r}_{3'}^{\text{in}})^{-\text{T}} \quad (19)$$

Then the reaction force at $O_{3'}$ under the action of input force F_{in} can be obtained as:

$$\mathbf{F}_{3'} = \mathbf{C}_{3'}^{-1}\mathbf{U}_{3'} \quad (20)$$

Finally, the output displacement can be calculated by

$$u_{\text{out}} = 2 \cdot \mathbf{F}_{3'}(2) \cdot \mathbf{C}_{R2}(2, 2) \quad (21)$$

And the displacement amplification ratio can be obtained as

$$\lambda = u_{\text{out}}/u_{\text{in}} \quad (22)$$

According to Eq. (16) and Eq. (22), the input stiffness and amplification ratio are obtained. The adopted PSA (Type PK4FA2H3P2, *Thorlabs Inc.*) has a free stroke S_{PSA} of 7 μm with a blocking force of 800 N, so its effective stiffness K_{PSA} can be derived as 114 N/μm. The output stroke S_{out} can be calculated by

$$S_{\text{out}} = S_{\text{PSA}} \cdot \frac{K_{\text{PSA}}}{K_{\text{PSA}} + K_{\text{in}}} \cdot \lambda \quad (23)$$

3.3. Structure parameter optimization

Based on Eqs. (12) and (23), the dependence of output stiffness and amplification ratio on the structure parameters of the designed tool can be obtained in Fig. 6. We focus on the neck thickness t and the bridge inclination height L_3. The material properties needed for the numerical study are as follows: Young's modulus $E = 210$ GPa, Poisson's ratio $v = 0.3$, density $\rho = 7.85 \times 10^3$ kg/m³, and yield stress $\sigma_s = 780$ MPa.

As demonstrated in Fig. 6, the amplification ratio and the output stiffness move in the opposite direction with the increase of structure parameters. The output stiffness in the y-direction (thrust direction) is more sensitive to the parameter change. Generally, an increase in the output stroke or amplification ratio is accompanied by a decrease in the output stiffness. It is not feasible to achieve the maximal values for all three variables simultaneously. In this study, the structure parameters are chosen to balance the requirements of large output strokes and sufficient output stiffness. The actual parameters are summarized in Table 1 with overall consideration of working performance, PSA capabilities, and structure machinability.

To verify the developed analytical models, we performed finite element analysis (FEA) on the structure using ANSYS. The model was set up according to the CAD model shown in Fig. 3. The simulated results of the nominal and effective amplification ratios, as well as the input and output stiffness, are listed in Table 2 and compared with those obtained from the analytical models. The predicted results from

Table 1
Structure parameters of the 2-D NRVCT.

Sym.	Value (mm)	Sym.	Value (mm)
b	5.00	L_1	1.00
t	0.20	L_2	5.85
R	0.25	L_3	0.40
w_1	0.25	L_4	2.50
w_2	0.25	L_5	1.90
h_1	1.00	L_6	1.00
h_2	4.50	L_7	1.00
l_0	8.90	L_8	3.10

Table 2
Comparison between the FEA and analytical results.

Methods	λ	K_{in} (N/μm)	$S_{\text{out}}/S_{\text{PSA}}$	K_{out}^x (N/μm)	K_{out}^y (N/μm)
FEA	3.07	62.5	1.98	0.42	1.51
Models	3.17	63.8	2.03	0.41	1.50
Difference (%)	3.3%	2.1%	2.5%	−2.4%	−0.7%

the analytical models and FEA are very close with a maximal difference of 3.3%. The effective amplification of one bridge-type amplifier is around 2.0 which includes the effects of input and output stiffness, PSA capabilities and preload bolts. The output stiffness in the cutting direction reaches 0.4 N/μm, while the more critical output stiffness in the thrust direction is 1.5 N/μm, which all satisfy the design requirements.

3.4. Modal analysis

Another critical factor that limits tool bandwidth is the structure's first resonant frequency. Ideally, the tool operates only within the first resonant frequency to obtain a constant amplification ratio. In addition, the first two resonant modes would preferably match the cutting and thrust directions, so undesired parasite motions would not be excited. The modal analysis results from FEA are shown in Fig. 7, where the first resonant mode is in the cutting direction and the natural frequency is at 6, 452 Hz; and the second resonant mode is in the thrust direction while the natural frequency is at 7, 432 Hz. Both frequencies exceed the targeted bandwidth (6 kHz). Additional dynamic tests regarding the frequency response are presented in the next section.

Structural analysis was performed to study the stress state of the design under extreme working conditions. When the maximal input voltage 150 V was used to actuate the PSAs statically, the maximum effective stress of 270 MPa was observed at the RCFH. It is much smaller than the spring steel's yield strength of 780 MPa, which ensures that the tool deformations are all within the elastic range.
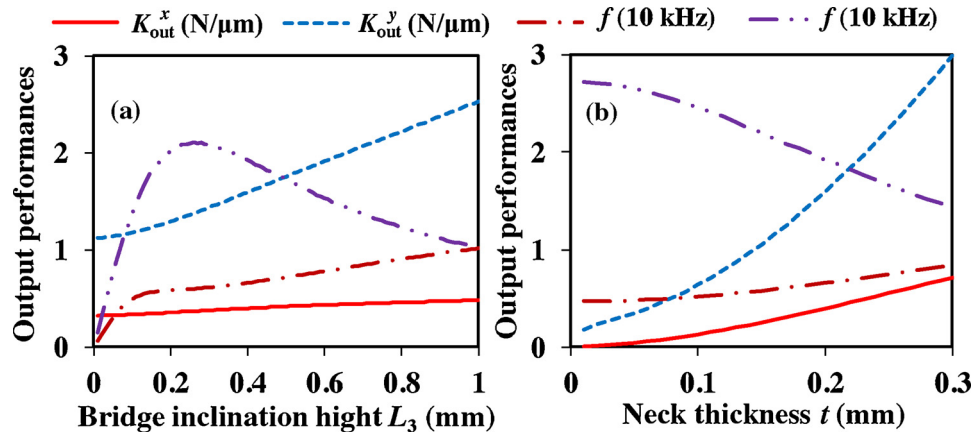

Fig. 6. Effects of the structure parameters of bridge-type amplifier on the working performances of 2-D NRVCT.
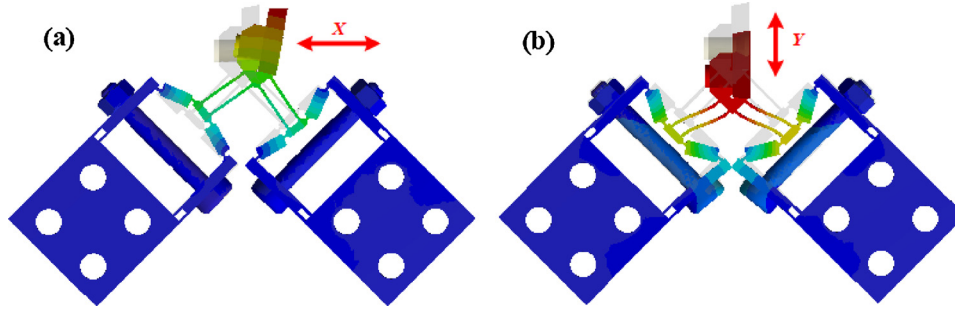
Fig. 7. Modal analysis results: (a) first resonant mode at 6452 Hz and (b) second resonant mode at 7432 Hz.

3.5. Drive current

To drive a capacitive load such as a PSA, the required current is proportional to the operating frequency, capacitance, and voltage amplitude. For a simple sinusoidal excitation, the required peak current I_{0-p} can be estimated as

$$I_{0-p} = \pi \cdot f \cdot C_{PSA} \cdot U_{p-p} \leq I_m \tag{24}$$

where f is the excitation frequency; C_{PSA} is the PSA capacitance; and U_{p-p} is the peak-to-peak voltage.

The peak current should not exceed the maximum permitted value I_m of the piezo voltage amplifier, while the excitation frequency should be within the signal bandwidth of the piezo amplifier. In this study, a commercial piezo voltage amplifier (P X 200, *PiezoDrive*) is used with a peak current capacity of 2A and a signal bandwidth of 390 kHz. The piezo stack actuator (Type PK4FA2H3P2, *Thorlabs Inc.*) has a dimension of 5 mm × 5 mm × 8.9 mm, a maximum stroke of 7 μm at 150 V, and a capacitance of 560 nF. Based on Eq. (24), the relationships between the maximal output strokes, the excitation frequency, and the required drive current are plotted in Fig. 8(a). When under pure sinusoidal excitation, the piezo actuator could achieve its maximal stroke up to 7.5 kHz, which is larger than its design bandwidth or its first natural frequency. It should be noted that a 2-D arbitrary trajectory is possible given that all frequency components of the signal are within the structure's natural frequency (around 6 kHz).

The drive current also determines the heat generation in the PSA due to dielectric loss, which is another big constraint for high-frequency operation of a piezo stack. From the manufacturer's data, the adopted PSA could maintain a temperature increase of < 40 °C under the full swing of operation at 6 kHz without active cooling [23]. Fig. 9 shows the experimentally measured temperature profile of PSA at high-frequency operation using an infrared thermometer. The temperature increases rapidly and reaches a stable value of 34 °C very soon after 80 s.
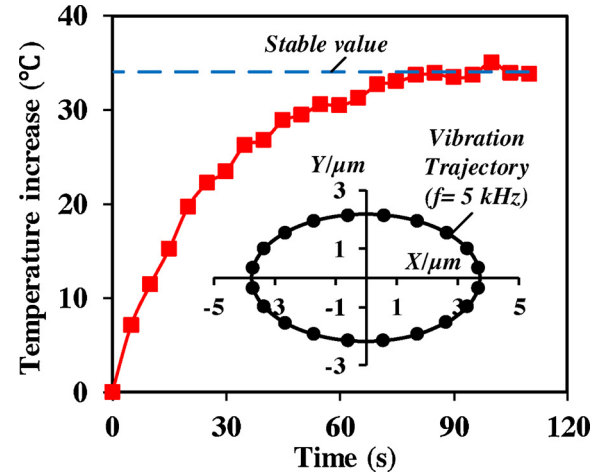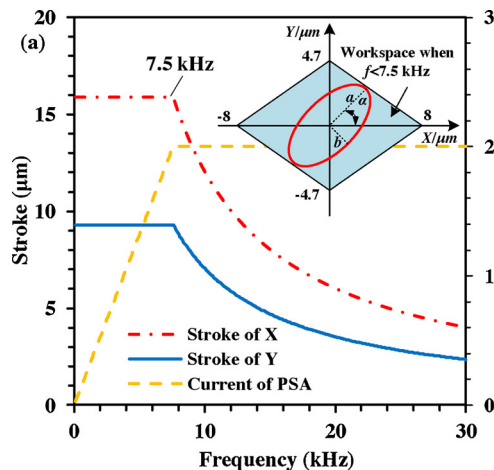

Fig. 9. Temperature increase of PSA at high-frequency operation.

The quick heat balancing also helps to maintain the cutting accuracy

4. Experimental evaluation of working performance

4.1. Coupling, hysteresis, and dynamic tests

One prototype tool was fabricated from a monolithic piece following the optimized structure parameters summarized in Table 1. As shown in Fig. 8(b), during the tests, excitation voltage signals were applied to the PSAs, while the responses of tip motion along the cutting and thrust directions were measured using a pair of capacitance sensors (Model 5504, *MicroSense*) with a measurement block, which was designed to have a same mass as the cutting insert. As shown in Fig. 3, the
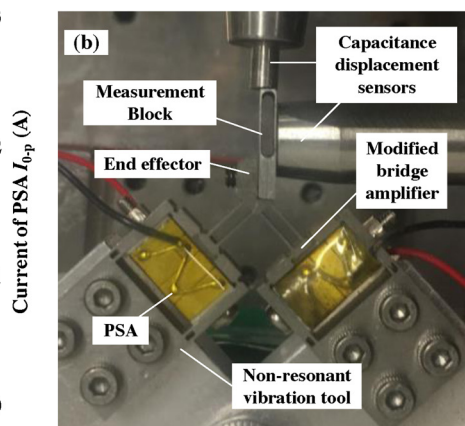

Fig. 8. (a) Relationship among PSA stroke, frequency and driving current; and (b) experimental setup for tool trajectory measurement.
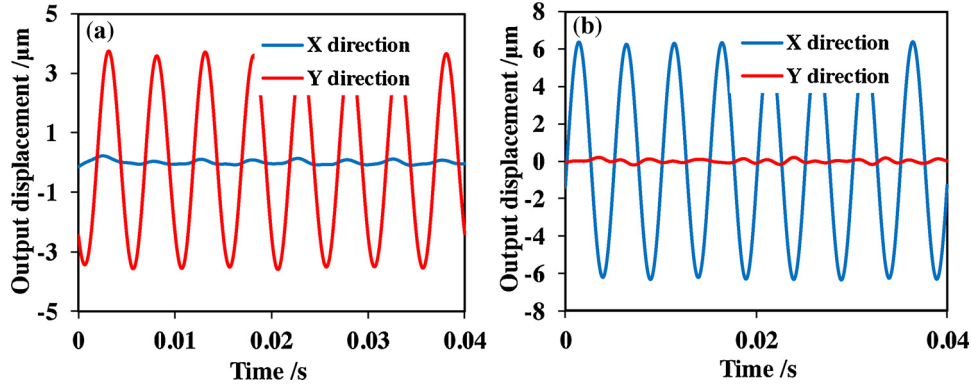
Fig. 10. On-machine coupling tests in the *X*- and *Y*-directions.

amplified motions from the PSAs are not aligned with the cutting and thrust directions, namely the *x* and *y* directions. The dependency of the two-directional motions u_{out}^x and u_{out}^y on the input voltages of PSAs can be expressed as:

$$\begin{bmatrix} u_{out}^x \\ u_{out}^y \end{bmatrix} = \begin{bmatrix} A_x & -A_x \\ A_y & A_y \end{bmatrix} \begin{bmatrix} U_0 + U_L(t) \\ U_0 + U_R(t) \end{bmatrix} \tag{25}$$

where $U_L(t)$ and $U_R(t)$ denote the voltage inputs of the left and right PSAs respectively; U_0 is the voltage offset to guarantee that resultant voltage input is always positive; A_x and A_y are the coefficients that transform the input voltages to output displacement.

First, coupling tests were performed by using two sinusoidal signals of 200 Hz for both PSAs. The two inputs have an identical amplitude of 120 V. The phase was set to 0 for pure thrust motion and 180° for pure cutting motion. Fig. 10 shows the results of the coupling effect between the two motions. It can be found that the coupling ratios in the *X*- and *Y*-directions are both within 5%. It can also be calibrated from the results that A_x = -0.053 μm/V and A_y = -0.031 μm/V.

Then, when the applied voltage amplitudes were increased from 0 to 120 V and back to 0 V linearly with respect to time, one can obtain the hysteresis property of the developed tool. The dependence of the *Y*-directional output displacement on the input voltage is shown in Fig. 11, from which a good linear relationship can be found.

Finally, the frequency sweep tests were performed by setting the input voltage amplitudes to 5 *V* and the frequency swept from 0 to 10 kHz linearly. The obtained amplitude-frequency and phase-frequency characteristics are illustrated in Fig. 12, from which the first and second natural frequencies in the *X*- and *Y*-directions are identified at 6100 and 7100 Hz, respectively. The results are also in good
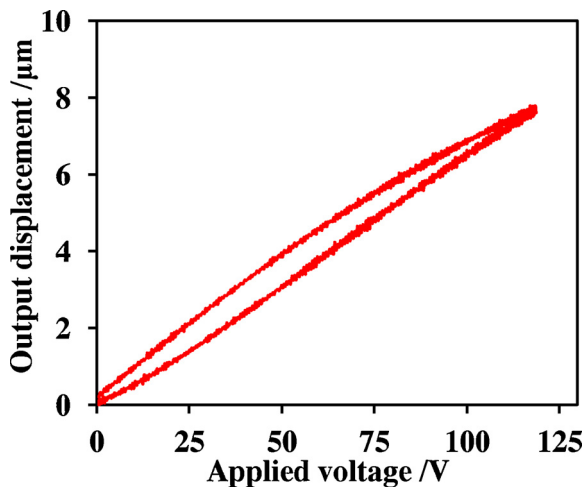
accordance with the FEA results of 6452 and 7432 Hz. Meanwhile, the phase difference has a linear relationship with the frequency and reaches the maximum value of 30° within the working bandwidth of 6 kHz. This ensures the controllable generation of elliptical trajectory within its working bandwidth. It is noteworthy to mention that developed tool has a much higher natural frequency than most of other existing 2-D non-resonant tools, as well as being capable of providing adjustable large amplitudes without extra cooling.

4.2. Elliptical trajectory generation

The elliptical vibration trajectory has a great impact on texturing performance. In order to generate arbitrary elliptical trajectories in the workspace, the relationship between the designed elliptical trajectory and the input voltages are required to be clarified. Fig. 8 shows an arbitrary elliptical trajectory, which is an oblique ellipse in the *XY* coordinate system. As shown in Fig. 8, the half-lengths of the long and short axes of the oblique ellipse are denoted by *a* and *b* respectively. The inclination angle of the oblique ellipse is *α*. One can completely define an elliptical trajectory by giving *a*, *b* and *α*.

According to the ellipse equations, the relationship between the input voltage (U_L, U_R and ϕ) and elliptical trajectory parameters (*a*, *b* and *α*) can be derived as:

$$\begin{cases} |A_x| = \dfrac{\sqrt{a^2 \cos^2\alpha + b^2 \sin^2\alpha}}{\sqrt{U_L^2 + U_R^2 - 2U_L U_R \cos\phi}} \\[2mm] |A_y| = \dfrac{\sqrt{a^2 \sin^2\alpha + b^2 \cos^2\alpha}}{\sqrt{U_L^2 + U_R^2 + 2U_L U_R \cos\phi}} \\[2mm] \dfrac{2U_L U_R \sin\phi}{U_L^2 - U_R^2} = \dfrac{2ab}{\sin 2\alpha(a^2 - b^2)} \end{cases} \tag{26}$$

The corresponding input voltage can be numerically calculated using Eq. (26) for any designed elliptical trajectory in the workspace. In order to verify the controllability of elliptical vibration using the developed 2-D NRVCT, eight sets of elliptical trajectories with different inclination angles were generated based on Eq. (26). The eight sets include a perfect circle with a radius of 2 μm, five ellipses with the same semi-major and semi-minor axes of 3 μm and 1 μm but different inclination angles of 0°, 45°, 90° and 135°, and two ellipses with the same semi-minor axis of 2.5 μm but different semi-major axes of 6.5 μm and 4 μm and different inclination angles of 0° and 90° respectively.

The tests were performed for both the low-frequency (200 Hz) and high-frequency (5.5 kHz) operations with the results plotted in Fig. 13. The results demonstrate a good agreement between the designed and measured trajectories at the low frequency. The discrepancy between the designed and measured trajectories increases at the higher frequency mainly due to the linearly increasing phase shift, as shown in Fig. 12(b). We here demonstrate only the actual open-loop performance showing the system characteristics. The deviation of trajectories could
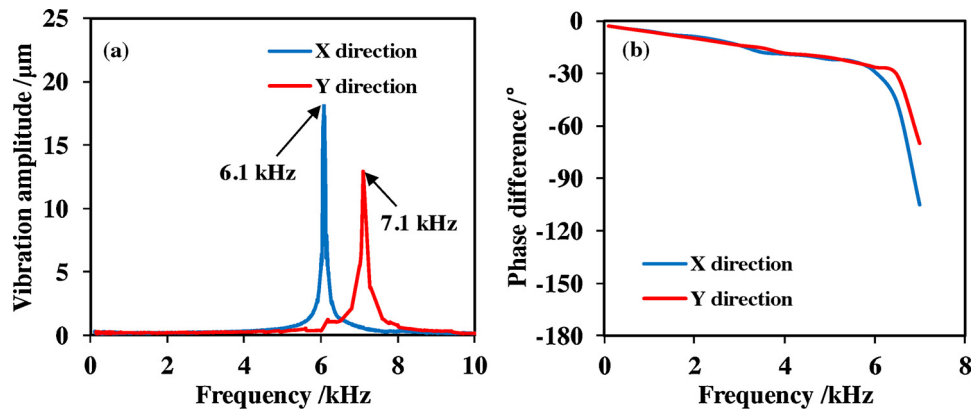

Fig. 11. On-machine hysteresis test.

Fig. 12. Frequency response of the (a) amplitude and (b) phase in the *X*- and *Y*-directions.
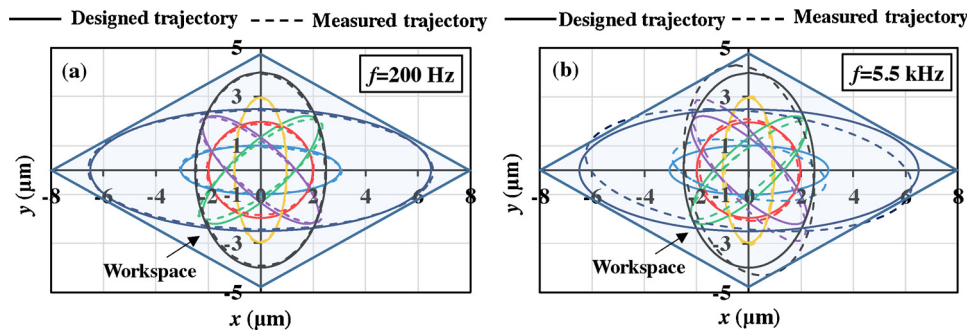

Fig. 13. Comparison between the designed and measured elliptical trajectories of 2-D NRVCT at (a) 200 Hz and (b) 5.5 kHz.
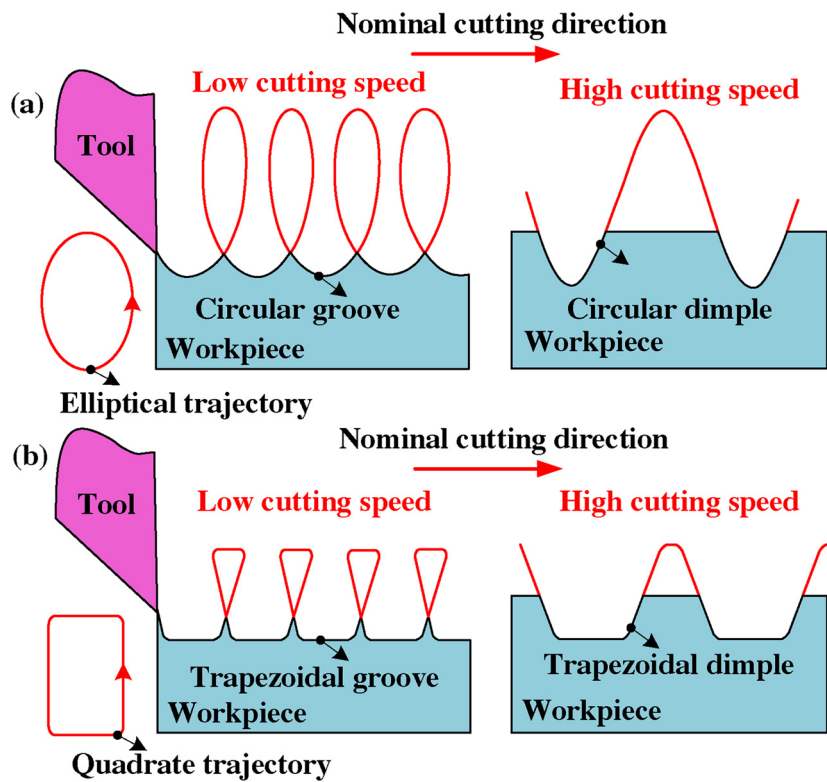

Fig. 14. Principle of vibration texturing process with the (a) elliptical and (b) quadrate trajectories.

be eliminated through frequency compensation.

4.3. Surface texturing tests

The direct application of developed 2-D NRVCT is in surface texturing for fast generation of micro-structured surfaces. Here we
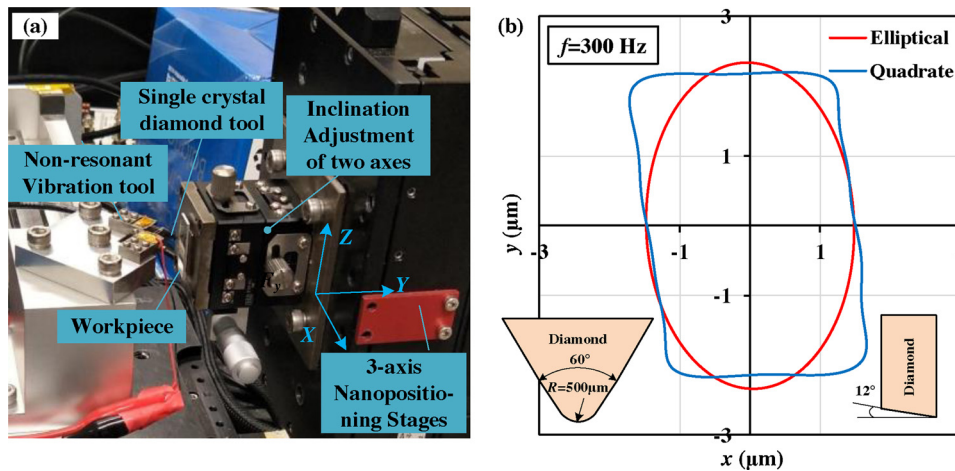
Fig. 15. (a) Experimental setup of 2-D NRVCT for surface texturing and (b) measured vibration trajectories.
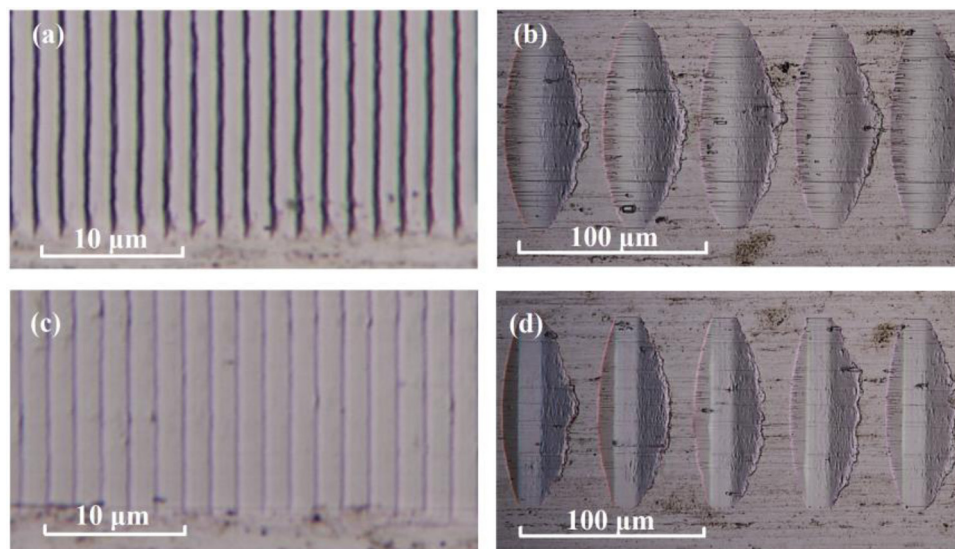

Fig. 16. Topography of textured surfaces with the elliptical trajectory at 300 Hz: (a) cutting speed of 0.6 mm/s and (b) cutting speed of 15 mm/s; and with the quadrate trajectory at 300 Hz: (c) cutting speed of 0.6 mm/s and (d) cutting speed of 15 mm/s.

demonstrate two typical cases of surface texturing with the elliptical and quadrate trajectories. Fig. 14(a) demonstrates the conventional elliptical vibration texturing which can also be achieved by a resonant-type tool. By utilizing a low cutting velocity, the overlapping trajectories can generate micro-grooves on the substrate; while a higher cutting velocity results in non-overlapping trajectories to generate discrete circular dimple structures. Fig. 14(b) shows the unique capability of proposed 2-D NRVCT to machine micro-structures with an arbitrary tool trajectory thanks to its high working bandwidth. It gives the flexibility to precisely control the cross-section profiles of machined features, which is a critical factor in determining their functional performance. When a quadrate trajectory is employed, we can generate parallel grooves and dimples with a trapezoidal profile as shown in Fig. 14(b). These kinds of structured surfaces could find their potential applications in microfluidic device, surface wettability control, cell attachment, etc.

The experimental setup for surface texturing is shown in Fig. 15(a). The 2-D NRVCT is mounted on a direct-drive linear actuator (ACT165DL, *Aerotech*), which is used to generate the nominal cutting motion with respect to the workpiece. The workpiece is aluminum alloy with a dimension of 2 mm × 10 mm × 30 mm. It was glued to a two-degree-of-freedom tilt stage, which could be used for level adjustment. The title stage was mounted on a three-axis nano-positioning stage

(ANT130XY and ANT130LZ, *Aerotech*), which is used to generate relative feed motion. A natural single crystal diamond insert provided by *Contour Fine Tooling* has a nose radius of 500 μm, a rake angle of 0°, and a clearance angle of 12°. A digital camera was used for tool setting.

In the first set of experiments, the elliptical trajectory was generated at 300 Hz. In the second set of experiments, the quadrate trajectory was generated at 300 Hz. The input voltage signals to generate a perfect quadrate shape must include frequency components of infinite orders. In order to minimize output distortion in the quadrate trajectory generation, the input signals were filtered by a low pass filter with a cut-off frequency at 3 kHz before applied to the PSAs. These two kinds of 2-D vibration trajectories were measured before texturing tests and are shown in Fig. 15(b). The nominal cutting velocity was set to 0.6 mm/s for both cases to generate overlapping trajectories for machining parallel grooves (Fig. 16(a) and (c)); while the cutting speed was set to 15 mm/s for machining discrete dimple structures shown in Fig. 16(b) and (d). The machined surfaces were measured using a digital microscope (RH-2000, *Hirox*) and an optical surface profiler (*Zygo*), which are shown in Figs. 16 and 17 respectively.

Another unique application of developed 2-D NRVCT utilizing its wide bandwidth is modulated elliptical vibration texturing of microstructured surfaces. Fig. 18(a) shows the principle of modulated elliptical vibration texturing, in which an additional modulation motion is
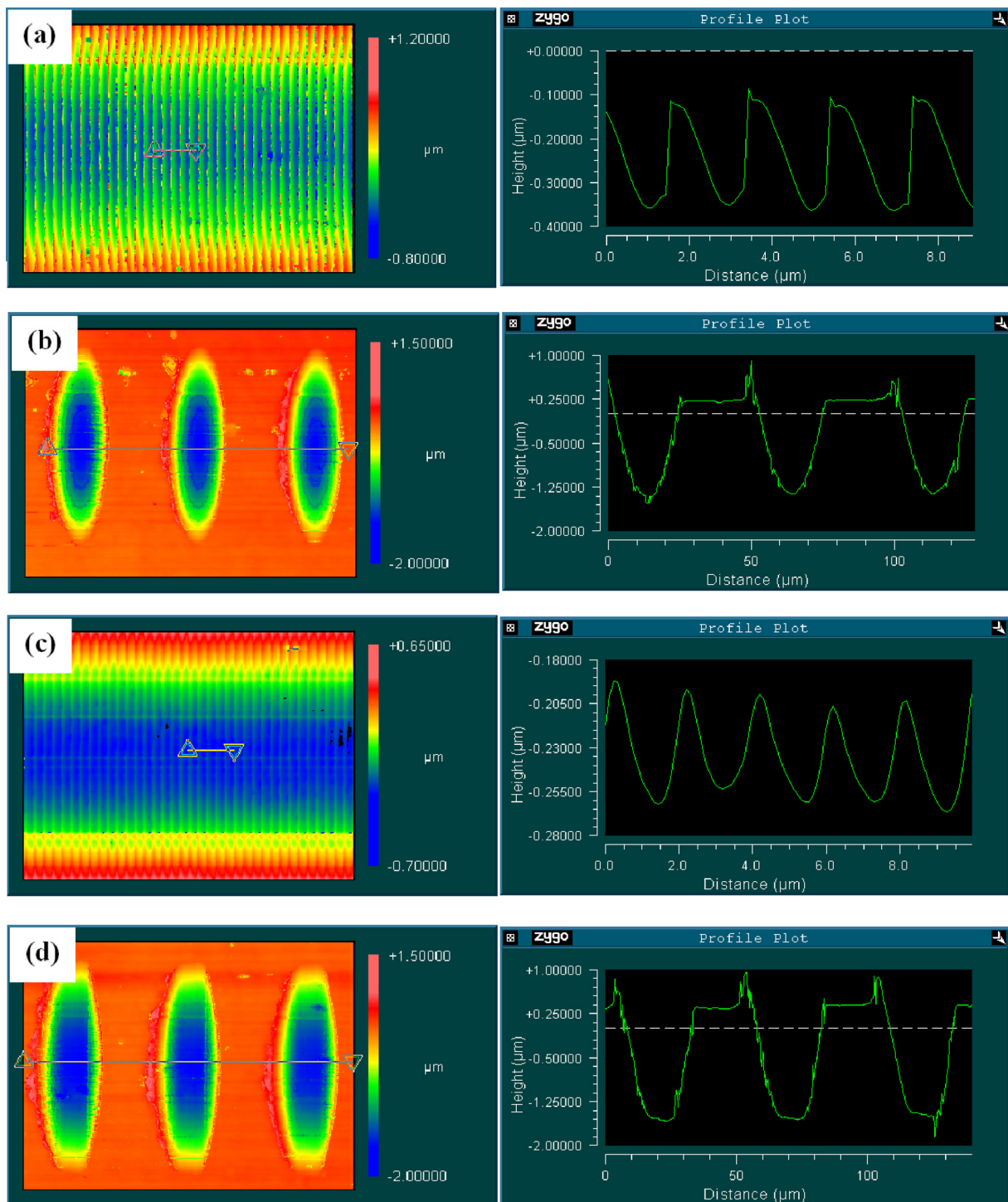
Fig. 17. Surface profile measurement for the (a) circular grooves; (b) circular dimples; (c) trapezoidal grooves; and (d) trapezoidal dimples.

superimposed on the elliptical vibration to dynamically adjust its vibration center along the depth-of-cut direction. The elliptical vibration is used to improve material machinability, while the modulation motion is used to generate the surface profile of micro-structures. The proposed ultrafast 2-D NRVCT is capable of simultaneous generation of an arbitrary low-frequency modulation motion and a high-frequency of elliptical vibration owing to its wide bandwidth. Here we demonstrate a typical test of modulated elliptical vibration texturing. In the test, harmonic waveform modulated elliptical vibration was generated with measurement results shown in Fig. 18(b). The elliptical trajectory of the high-frequency vibration was set to be a perfect circle of 1 μm radius at

3500 Hz, while the low-frequency modulation motion was set to be a sinusoidal waveform of $3\,\mu m_{0-p}$ at 20 Hz. The nominal cutting speed was set to be 1 mm/s; the nominal depth of cut was set to be 6 μm. The machined surfaces were measured using the digital microscope (RH-2000, *Hirox*), which are shown in Fig. 19. Compared with the direct vibration texturing results in Fig. 16(b) and Fig. 16(d), the edge burr of micro-structures in Fig. 19 were significantly reduced with the utilization of modulated elliptical trajectories.
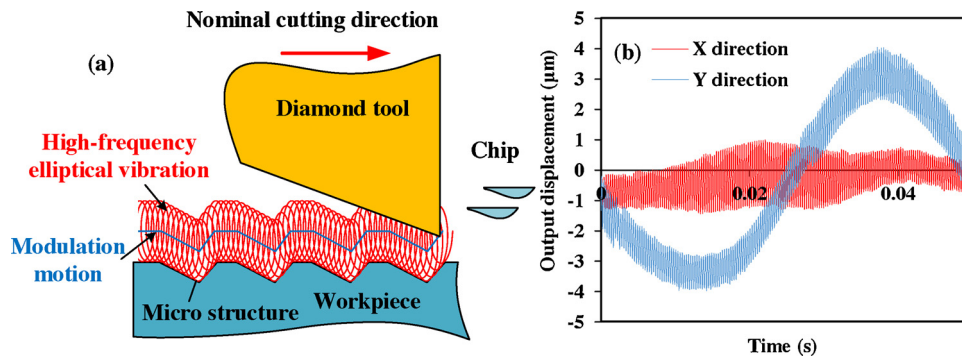
Fig. 18. (a) Principle of modulated elliptical vibration texturing; and (b) measured tool vibration trajectories.
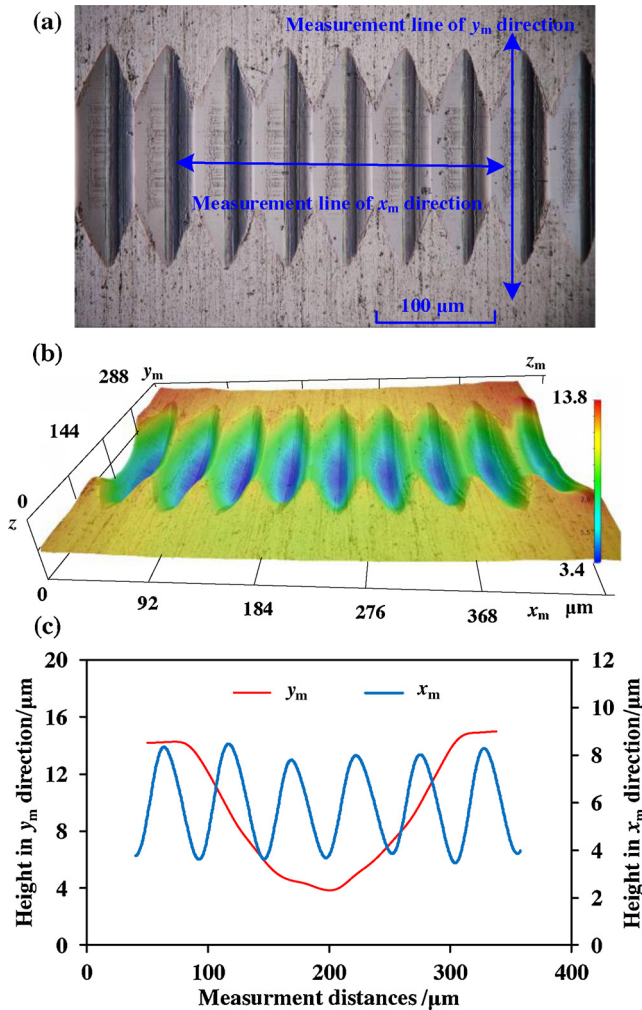

Fig. 19. Machined structures of modulated elliptical vibration texturing: (a) microphotograph; (b) 3D topography; (c) sectional profile in x_m-direction and y_m-direction.

5. Conclusions

This study presents the development of an ultrafast 2-D non-resonant vibration cutting tool (NRVCT) for machining micro-structured surfaces. The tool is capable to operate at up to 6 kHz in a workspace of 9.3 μm × 16 μm without extra cooling. The output stiffness reaches 0.4 N/μm in the cutting direction and 1.5 N/μm in the thrust direction. The coupling between the motions of two axes is within 5%. The tool performance has been analytically modeled and verified by finite element simulation and experiments. In addition, we have demonstrated

surface texturing results with the elliptical, quadrate and modulated elliptical trajectories using the proposed tool. Beyond this specific tool design, we have also presented a general design guideline and modeling techniques for flexure-hinge based 2-D tool design for high-frequency operation. Some more general conclusions can be drawn as follows.

(1) The design requirements of 2-D NRVCT for high-frequency operation can be summarized as five design specifications, including the output stroke, stiffness, first natural frequency, coupling coefficient and drive current. Very often, these five specifications are mutually restricted, which need to be balanced based on the specific performance requirements.

(2) In order to operate at a high frequency with low heat generation and low current requirement, the capacitance of PSAs must be strictly limited (below 1 μF). The piezo stack thus usually cannot provide enough stroke directly. A mechanical amplification mechanism is needed to amplify the displacement output. The introduction of the amplification mechanism, however, will decrease the output stiffness and the structure resonant frequency. The approach adopted in the proposed design is to utilize a modified bridge-type mechanism with a small amplification ratio to balance the requirements among the stroke, output stiffness, resonant frequency, and drive current.

(3) For flexure-hinge based design, the compliance matrix method is an effective and reliable method for modeling the output stroke and stiffness, which can also take into account the stiffness of PSAs and preloading bolts. We have demonstrated the detailed modeling procedures to apply the compliance matrix method.

(4) The bandwidth of 2-D NRVCT is limited by its first structural resonant frequency as well as the maximal drive current of the piezo amplifier. Ideally, the first two resonant modes of the structure are in accordance with the two major vibration motions, so when the tool is excited near the resonant frequency, no parasite motions are excited. The drive current is proportional to the capacitance, excitation voltage, and frequency, so it is possible to have a larger workspace at a lower operating frequency, and a smaller workspace at a higher frequency limited by the current capability. In addition, the heat generation needs to be carefully checked for long-term operation.

(5) The unique capability of developed 2-D NRVCT is to generate arbitrary tool trajectories instead of only harmonic excitations. The frequency contents of the arbitrary excitation signals need to be limited within the bandwidth of the tool. We have demonstrated in this paper the surface texturing of micro-dimples and grooves with controlled cross-section profiles using both the elliptical and quadrate tool trajectories.

(6) Another unique capability of developed 2-D NRVCT is to generate high-frequency elliptical vibration and low-frequency modulation motion simultaneously thanks to its wide bandwidth. The high-frequency elliptical vibration is utilized to improve the material

machinability, while the modulation motion is applied to generate the surface profile of micro-structures. We have demonstrated in this paper the surface texturing of micro-grooves with reduced edge burr using modulated elliptical trajectories.

Declaration of Competing Interest

The authors declare that there are no conflicts of interest.

Acknowledgments

References

[1] Kim DE, Cha KH, Sung IH, Bryan J. Design of surface micro-structures for friction control in micro-systems applications. CIRP Ann Manuf Technol 2002;51:495–8.
[2] Whitesides GM. The origins and the future of microfluidics. Nature 2006;442:368–73.
[3] Brandner JJ, Anurjew E, Bohn L, Hansjosten E, Henning T, Schygulla U, et al. Concepts and realization of microstructure heat exchangers for enhanced heat transfer. Exp Therm Fluid Sci 2006;30:801–9.
[4] Fang FZ, Zhang XD, Weckenmann A, Zhang GX, Evans C. Manufacturing and measurement of freeform optics. CIRP Ann Manuf Technol 2013;62:823–46.
[5] Bruzzone A, Costa HL, Lonardo PM, Lucca DA. Advances in engineered surfaces for functional performance. CIRP Ann Manuf Technol 2008;57:750–69.
[6] Kong X, Dong J, Cohen PH. Modeling of the dynamic machining force of vibration-assisted nanomachining process. J Manuf Process 2017;28:101–8.
[7] Dubey AK, Yadava V. Laser beam machining-a review. Int J Mach Tool Manuf 2008;48(6):609–28.
[8] Guo P, Ehmann KF. Development of a tertiary motion generator for elliptical vibration texturing. Precis Eng 2013;37:364–71.
[9] Dornfeld D, Min S, Takeuchi Y. Recent advances in mechanical micromachining. CIRP Ann Manuf Technol 2006;55:745–68.
[10] Hong MS, Ehmann KF. Generation of engineered surfaces by the surface-shaping system. Int J Mach Tool Manuf 1995;35:1269–90.
[11] Zhang J, Cui T, Ge C, Sui Y, Yang H. Review of micro/nano machining by utilizing elliptical vibration cutting. Int J Mach Tool Manuf 2016;106:109–26.
[12] Yang Y, Gao S, Chen K, Pan Y, Guo P. Vibration analysis and development of an ultrasonic elliptical vibration tool based on a portal frame structure. Precis Eng 2017;50:421–32.
[13] Ahn J, Lim H, Son S. Improvement of micro-machining accuracy by 2-dimensional vibration cutting. Proc ASPE 1999:150–3.
[14] Heamawatanachai S, Bamberg E. Design and characterization of a PZT driven micromachining tool based on single-point tool tip geometry. Precis Eng 2009;33:387–94.
[15] Negishi N. Elliptical vibration assisted machining with single crystal diamond tools. 2003.
[16] Zhu Z, Zhou X, Liu Z, Wang R, Zhu L. Development of a piezoelectrically actuated two-degree-of-freedom fast tool servo with decoupled motions for micro-/nano-machining. Precis Eng 2014;38:809–20.
[17] Lin J, Han J, Lu M, Yu B, Gu Y. Design, analysis and testing of a new piezoelectric tool actuator for elliptical vibration turning. Smart Mater Struct 2017;26:085008.
[18] Li Y, Xu Q. Design and analysis of a totally decoupled flexure-based XY parallel micromanipulator. IEEE T Robot 2009;25:645–57.
[19] Zhang J, Zhang J, Cui T, Hao Z, Zahrani A. Sculpturing of single crystal silicon microstructures by elliptical vibration cutting. J Manuf Process 2017;29:389–98.
[20] Zhu W, Zhu He Y, Ehmann KF, Ju Li S. Development of a novel 2-D vibration-assisted compliant cutting system for surface texturing. IEEE ASME Trans Mechatron 2017;22:1796–806.
[21] Yong YK, Lu T, Handley DC. Review of circular flexure hinge design equations and derivation of empirical formulations. Precis Eng 2008;32:63–70.
[22] Koseki Y, Tanikawa T, Koyachi N, Arai T. Kinematic analysis of translational 3-DOF micro parallel mechanism using matrix method. Adv Robot 2002;16(3):251–64.
[23] Thorlabs Inc. Discrete piezoelectric stacks with through hole. 2019 (Accessed 28 January 2019 https://www.thorlabs.com/newgrouppage9.cfm?objectgroup_id=10312.